Particle streak velocimetry and CH laser-induced fluorescence diagnostics in strained, premixed, methane-air flames

J. M. Bergthorson[†*], D. G. Goodwin[‡], and P. E. Dimotakis[†]

[†] *Graduate Aeronautical Laboratories,*
[‡] *Department of Mechanical Engineering,*
California Institute of Technology, Pasadena, CA, USA, 91125

Abstract

We present the use of simultaneous Particle Streak Velocimetry (PSV) and CH Planar Laser Induced Fluorescence (PLIF) diagnostics in the study of planar, strained, premixed, methane-air flames, stabilized in a jet-wall stagnation flow. Both PSV and PLIF data are imaged at high spatial resolution and sufficiently high framing rates to permit an assessment of flame planarity and stability. Concurrent measurements of mixture composition, (Bernoulli) static-pressure drop, and stagnation-plate temperature provide accurate boundary conditions for numerical simulations. The new PSV implementation is characterized by very low particle loading, high accuracy, and permits short recording times. This PSV implementation and analysis methodology is validated through comparisons with previous laminar flame speed data and detailed numerical simulations. The reported diagnostic suite facilitates the investigation of strained methane-air flames, as a function of nozzle-plate separation to jet-diameter ratio, L/d, and equivalence ratio, Φ. Flames are simulated using a one-dimensional streamfunction approximation, with full chemistry (GRI-Mech 3.0), and multi-component transport. In general, we find good agreement between experiments and simulations, if boundary conditions are specified from measured velocity fields. Methane-air flame strength appears to be slightly overpredicted, with the largest disagreements for lean flames.

1. Introduction

Planar, strained flames provide a valuable development and validation testbed for transport and kinetics models that can then be used in any combustion environment. The high parametric dimensionality of these models requires many detailed and accurate experiments over a sufficiently large range of conditions. Such experiments are enhanced by diagnostics that simultaneously permit detailed flow and chemical-species data to be measured and compared to model predictions. This paper describes a suite of diagnostics developed for this purpose and employed to probe planar, strained, methane-air flames, stabi-

lized in a jet-wall stagnation flow. This setup yields a flow with boundary conditions that can be accurately specified, facilitating simulation and comparisons with experiment. This flow can also, with care, be stable to high Reynolds numbers. The diagnostics are optimized for accuracy, minimal flame disturbance, and rapid simultaneous recording of flow velocity and CH radical profiles.

Diagnostics documented here include extensions to and improvements of Particle Streak Velocimetry (PSV), complemented by simultaneous CH Planar Laser Induced Fluorescence (PLIF) imaging at 10 Hz. PLIF spectroscopy confirms the CH excitation and helps optimize dye-laser wavelength for signal-to-noise ratio. PLIF images are processed to extract CH radical profiles and assess flame planarity. The 10 fps PLIF sequence permits an assessment of flame

---

*Corresponding author.
E-mail address:* `jeffb@tyrvos.caltech.edu`

stability under all conditions. Only data from stable flame conditions are included.

Particle Streak Velocimetry (PSV) [1–3], a technique similar to particle tracking velocimetry [4], is used for instantaneous flow-field measurements and, in particular, axial velocities along the flow centerline. In combustion, PSV was previously used for qualitative flow descriptions (*e.g.*, Sugiyama [5]). Extensions and improvements to PSV implemented here include digital imaging and processing, and new analysis techniques. The implementation yields a Lagrangian measurement of velocity that, in principle, requires only a single particle traversing a steady flame. The consequent PSV accuracy competes favorably with LDV and PIV techniques, while a 1-2 order of magnitude reduction in particle loading minimizes flame disturbances, and Mie-scattering and stray-light interference in PLIF images. Velocity data are used to specify boundary conditions for simulations and are compared to predictions.

The spatial distribution of the CH radical can be measured with PLIF. Its narrow spatial profile is well-correlated with flame location and provides a sensitive test of direct predictions of strained-flame models.

Simultaneous measurements of air, fuel, and diluent mass fluxes, as well as of stagnation plate temperature, allow an accurate specification of boundary conditions for simulations.

Experimental profiles are compared to one-dimensional simulation predictions, using the *Cantera* software package [6]. The simulations incorporate GRI-Mech 3.0 kinetics [7] with multi-component transport [8]. The simulations rely on a one-dimensional streamfunction formulation [9]. Few comparisons between this formulation and actual velocity data have been documented, however. Law and coworkers studied methane-air, opposed-jet flames for lean, stoichiometric, and rich mixtures, using LDV and CARS for velocity, temperature, and major-species measurements to quantify the effect of stretch on flame structure [10–13]. To compare experimental and simulated data, a potential-flow boundary condition with a variable inflow mass flux is used to visually match the profiles. The authors report general agreement for temperature and major species profiles when flame location is adjusted to match the measurements.

The new PSV methodology is validated by comparing extrapolated laminar flame speeds with existing data and numerical simulations. Slightly lean, strained, methane-air flames are studied as a function of the nozzle-stagnation plate separation distance, L, to assess the simplified hydrodynamic model. Flame temperature dependence is studied by mixture dilution with excess nitrogen. The diagnostics are applied to methane-air flames, under similar strain-rate conditions, as a function of equivalence ratio, Φ. The approach and diagnostics permit an assessment of the numerical simulation predictions of strained-flames.

2. Experiments

A room-temperature, atmospheric-pressure jet is generated from a contoured nozzle with an exit diameter of $d = 9.9$ mm that impinges on a constant-temperature (water-cooled) copper stagnation plate. Three K-type thermocouples are embedded on the centerline, spaced vertically between the stagnation and cooled surface, to allow monitoring of wall temperature and temperature gradients.

The pressure difference between the jet plenum interior and a point just outside the jet-core flow region is measured with a 1 torr full-scale differential-pressure transducer (BOC Edwards W57401100 and W57011419). The Bernoulli velocity, $U_{\mathrm{B}} = \sqrt{(2\,\Delta p)/(\rho[1 - (d/d_{\mathrm{P}})^4])}$, is then calculated, where Δp is the nozzle static pressure drop, ρ the fluid density, d the nozzle exit diameter, and d_{P} the plenum (inner) diameter. The Bernoulli velocity will be higher than the jet-exit velocity for $L/d \leq 1$, owing to a velocity defect produced by streamline curvature at the nozzle-exit [14].

Fuel, oxidizer, and nitrogen-diluent mass flow rates are set using sonic metering valves and monitored concurrently (Omega FMA868-V-Methane, FMA872-V-Air and FMA873-V-Air, calibrated using a Bios DryCal ML-500). Estimated uncertainty in the mass-flow measurement of the air and fuel streams is, approximately, 1%, each. Bernoulli pressure, mass-flow, and temperature data acquisition is synchronized with digital-image acquisition, allowing accurate specification of simulation boundary conditions.

2.1. Particle Streak Velocimetry (PSV)

Flow velocities along the jet centerline are measured using Particle Streak Velocimetry (PSV) [1–3]. The implemented PSV methodology yields low-fractional-error axial-velocity data. The resulting accuracy is comparable to that obtained with LDV or PIV, while offering several advantages in flame environments. The reduced particle loading required for PSV minimizes flame disturbances introduced by particle seeding that can alter the effective thermal/heat-capacity environment, or the chemical kinetic/catalytic environment by providing surface-chemistry sites. Low PSV particle loading also reduces Mie-scattering interference in CH PLIF image-data, improving CH profile statistics. Particle loading required for accurate velocity measurements with PSV is an order of magnitude lower, or more, than required for LDV, or PIV. In a single PSV image frame, one or two particles traversing the vertical extent of the imaged region can suffice. In contrast, PIV measurements require a dispersion of particles throughout the domain in any one (short-time) exposure. With LDV, high particle number densities are required for converged statistics in a reasonable time.

A single PSV image captures the entire velocity field, making it ideal for short-run-time experiments. An example PSV image for a stagnation flame is shown in Fig. 1a. In axisymmetric, steady

stagnation flow, axial velocities along the centerline can be reliably measured; particle paths do not cross or overlap, and occasional out-of-plane particle displacements are small and easily discernible (in-/out-of-focus streaks). The high sensitivity of the scattering cross section to particle size, in the size range employed, allows easy identification of agglomerates that may not track high spatial-gradient regions in the flow. Streaks used for PSV processing are from in-plane, non-agglomerated particles. In a variable-velocity field, particles track the flow if the dimensionless product of the local strain rate, $\sigma = \partial u/\partial x$, and the Stokes time, $\tau_S \equiv \rho_p d_p^2/(18\,\mu)$, is small, $i.e.$, provided $\sigma \tau_S \ll 1$. The measurements relied on alumina particles ($\mathrm{Al_2O_3}$; median size, $d_p \cong 0.8\,\mu$m, $\rho_p \cong 3830\,\mathrm{kg/m^3}$; Baikowski Malakoff, RC-SPT DBM). For the strain rates in these experiments, $\sigma \tau_S \leq 3 \times 10^{-3}$.

A Coherent I-90 $\mathrm{Ar^+}$ laser, operated at $2-3\,$W, provides the PSV illumination source. Two cylindrical lenses generate a thin laser sheet ($\approx 200\,\mu$m) in the field of view. An Oriel (Model 75155) chopper with a 50% duty-cycle wheel modulates the laser beam. The chopper wheel is placed at a laser-beam waist to minimize on-off/off-on transition times. Chopping frequencies are in the range, $1.6\,\mathrm{kHz} \leq \nu_c \leq 2.4\,\mathrm{kHz}$, with ν_c optimized depending on flow velocity.

PSV image data are recorded using the in-house-developed "Cassini" digital-imaging system that relies on a low-noise, 1024^2-pixel CCD, with a (square) $12\,\mu$m pitch. A PSV image frame rate of 4 fps is chosen to further minimize particle-loading requirements. Magnification ratios are in the range of $1:1.0 - 1:1.5$ using a Nikon 105 mm, $f/2.8$ macro lens (with a 514.5 nm bandpass filter).

Local velocities, $u(x)$, are estimated from streak pairs as, $u(x) \cong \Delta X(x)/\Delta t$, yielding $u_I = L_I/\tau_c$ and $u_{II} = L_{II}/\tau_c$, where $\tau_c = 1/\nu_c$ (reciprocal of chopper frequency) and $L_I = x_{2s} - x_{1s}$ and $L_{II} = x_{2e} - x_{1e}$ are the distances from the start/end of one streak to the start/end of the next, respectively ($cf.$ Fig. 1b). Using the same intensity threshold on a streak pair removes systematic errors in applying the Lagrangian time interval, τ_c. This methodology is spatially second-order accurate and produces good agreement between velocity values derived from each streak pair. Streak lengths are estimated using bicubic fits on the 2-D streak-intensity image data, sampled to a 0.1-pixel resolution in both dimensions. An intensity threshold of ≈ 0.3 of the maximum intensity of each streak is used. The results do not depend on this choice and yield an rms error of $\approx 0.01\,U_j$, where U_j is the jet-exit velocity.

The velocity estimate, u_I, is located at $x_I = (x_{1s} + x_{2s})/2 + (w_1 + w_2)/4$, where x_{is} is the spatial location of the start of the ith streak and w_i is the width of the ith streak ($cf.$ Fig. 1b). Similarly, u_{II} is located at $x_{II} = (x_{1e} + x_{2e})/2 - (w_1 + w_2)/4$, where x_{ie} is the location of the end of the ith streak. PSV spa-

tial resolution is comparable to that of other particle velocimetry techniques, $e.g.$ PIV, LDV, that rely on comparable spatial displacements ($e.g.$, $10 - 30\,$pix, or $\approx 100 - 300\,\mu$m, for this flow). These methods measure the distance traveled by a particle along a Lagrangian path in a fixed time (PIV, PSV), or the time required to traverse a number of fringes in space (LDV). Particle methods require care in regions of high fractional change in speed along individual particle track segments, here limited to measurements very close to the wall, or in regions of high velocity curvature.

2.2. Planar Laser Induced Fluorescence (PLIF)

CH fluorescence measurements are obtained by exciting the $Q_1(7)$ transition of the $B^2\Sigma - X^2\Pi(0,0)$ CH band at 390.30 nm, in the UV [15]. The UV beam is obtained from a tripled Nd:YAG (355 nm)-pumped dye laser (Spectra-Physics PRO-290 & Sirah PrecisionScan). Pulse duration is $\approx 5\,$ns with a linewidth of $\approx 0.1\,\mathrm{cm^{-1}}$ (1.5 pm). Fluorescence is recorded from the $A-X(1,1)$, $A-X(0,0)$, and $B-X(0,1)$ bands in the $420 - 440\,$nm range. Excitation to the B state yields a higher signal than excitation to the A state [16] and a large wavelength shift between excitation and fluorescence, facilitating filtering of Mie- and Rayleigh-scattering interference, which is important in particle-seeded flames. The $Q_1(7)$ band provides a high signal level and low temperature sensitivity.

The output of the dye laser is passed through a pair of cylindrical lenses (150 mm and 500 mm at right angles) and yields a laser sheet with a Rayleigh range centered on the jet axis. Fluorescence is collected with a Nikkor 50 mm, $f/1.2$ lens at magnifications near 1:1, with a Schott KV-418 long-pass filter to reject scattering of the UV laser illumination, while transmitting approximately 90% of the fluorescence near 430 nm. Detection relies on a lens-coupled intensifier (Ultra-Blue Gen-III, Cooke Corp. VS-364) with a cooled CCD (Cooke Corp. SensiCAM^{QE}, binned to $344 \times 260\,\mathrm{pix^2}$; a binned pixel maps into $46\,\mu$m in the flow). A 70 ns gate time rejects chemiluminescence while retaining fluorescence. For the PLIF profiles presented here, a laser power of $\approx 10\,$mJ/pulse results in a saturated laser spectral intensity of $I_\nu = E_p/(\tau_p A_b SW) \approx 10^8\,\mathrm{(W/cm^2)/cm^{-1}}$, where E_p is the pulse energy, τ_p the pulse length, A_b the laser beam cross-sectional area, and SW the laser spectral width [17]. A sample CH PLIF (single-exposure) image is reproduced in Fig. 2a, and an average of 1000 exposures is shown in Fig. 2b. To correct for dark current and Rayleigh scattering, an averaged image of the laser sheet (no flame) is subtracted from the image data. CH profiles are obtained from single-shot images by summing across the (flat) central portion of the flame. Single-image 60-column averaging, about the jet axis, yields good profile statistics.

Figure 3 shows an experimentally measured CH excitation scan, at a resolution of 0.5 pm. Spectrum simulations are performed with LIFBASE [18]. This

scan was recorded with a laser power of 0.2 mJ/pulse, in a 1mm×2cm sheet, producing a partially saturated laser spectral intensity of $I_\nu \approx 2 \times 10^6 \approx I_\nu^{\mathrm{sat}} \approx 10^6 \ (\mathrm{W/cm^2})/\mathrm{cm}^{-1}$.

3. Numerical method

Stagnation flame simulations are performed using the *Cantera* reacting-flow software package [6]. The one-dimensional solution for stagnation flows approximates the flow in terms of a streamfunction, $\psi(x, r) = r^2 U(x)$, with $U(x) = \rho u/2$, where u is the axial velocity [9]. The axisymmetric momentum equation then becomes,

$$2U\frac{\mathrm{d}}{\mathrm{d}x}\left(\frac{1}{\rho}\frac{\mathrm{d}U}{\mathrm{d}x}\right) - \frac{1}{\rho}\left(\frac{\mathrm{d}U}{\mathrm{d}x}\right)^2 - \frac{\mathrm{d}}{\mathrm{d}x}\left[\mu\frac{\mathrm{d}}{\mathrm{d}x}\left(\frac{1}{\rho}\frac{\mathrm{d}U}{\mathrm{d}x}\right)\right] = \Lambda \,. \quad (1)$$

In this formulation, $\Lambda = (1/r) \, \mathrm{d}p/\mathrm{d}r$ must be a constant. By treating Λ as unspecified, four boundary conditions are imposed on this third-order ordinary differential equation at $x = 0$ and $x = \ell$, with $0 < \ell \leq L$ a suitably chosen interior point, permitting $U(0) = 0$, $U'(0) = 0$, $U(\ell) = U_\ell$, $U'(\ell) = U'_\ell$. Exploiting the (cold) outer-flow solution to Eq. 1, which is a parabola, a quadratic is fit to the cold flow data upstream of the flame. U_ℓ and U'_ℓ are then calculated from the fit, at $x = \ell$, minimizing errors that could be introduced by an inconsistent specification of flow boundary conditions, or from differentiation of the raw data. Energy and species equations are also solved with specification of inlet composition, inlet temperature, and stagnation-wall temperature. A no-flux boundary condition for species is applied at the wall. The simulations use a multi-component transport model and the GRI-Mech 3.0 kinetics mechanism [7, 8]. Simulations of laminar flame speeds are performed using a freely propagating flame code with multi-component transport and the same kinetics mechanism [19].

4. Results and discussion

The PSV methodology is validated by comparing extrapolated laminar flame speed measurements with previous data and numerical simulations. Figure 4a plots sample reference flame speed and strain-rate data, and the extrapolated flame speed. Vertical error bars are based on linear regression techniques. Horizontal error bars represent the estimated uncertainty in Φ of 1.4%. Data at equivalence ratios of $\Phi = 0.75$, 0.84, and 0.95 are given in Fig. 4b, and compared to numerical simulations and previous LDV-based data [20, 21]. The measurements agree with previous data and, collectively, indicate lower flame speeds than predicted.

The diagnostic suite is applied to methane-air flames as a function of scaled separation distance, L/d, and Φ. Table 1 lists the equivalence ratio, scaled separation distance, and dilution for the experiments reported here. The first subset of experiments is at $\Phi \cong 1.0$, with variable L/d (Table 1a). A diluted

methane-air flame is also studied (Table 1b). Flame chemistry effects are probed at $L/d = 0.8$ by varying equivalence ratio and dilution (Table 1c). The dilution level is chosen to maintain similar stretch conditions as mixture-fraction is varied.

Figure 5 shows the results for a near-stoichiometric ($\Phi = 0.98$) methane-air flame, at $L/d = 0.6$. CH profiles, obtained from 60-column averages in single-exposure images, are normalized by peak values. The simulation predicts flame location with good agreement in both the flowfield and CH profile. Thermophoresis will cause a particle drift in the high temperature-gradient region of the flow [11]. Utilizing the simulated temperature profile, thermophoretic corrections yielded a maximum error of 3% in the high gradient region of the velocity profile (preheat zone). Velocity data in this region are used to visually assess simulation predictions and these (small) thermophoretic corrections are neglected; velocity data in the cold-flow region, where a quadratic is fit to determine flow boundary conditions, are unaffected by thermophoresis.

To compare simulations with experiments, the difference between measured and predicted peak CH concentration location, $x_{\mathrm{CH,PLIF}}$ and $x_{\mathrm{CH,sim}}$, scaled by the simulated CH layer thickness, δ_{CH}, is calculated. CH layer thicknesses are calculated as the Full Width at Half Maximum (FWHM) of Gaussian fits to simulated profiles. The difference between $x_{\mathrm{CH,PLIF}}$ and $x_{\mathrm{CH,sim}}$ is less than $0.1\,\delta_{\mathrm{CH}}$, in this case.

The scaled separation distance, L/d, is an important flow parameter. Figure 6 shows the results for a near-stoichiometric ($\Phi = 0.98$) methane-air flame, at $L/d = 0.8$. Predicted and experimental peak CH locations agree within $0.2\,\delta_{\mathrm{CH}}$ for $L/d = 0.6$, 1.0 and 1.2, and within $2\,\delta_{\mathrm{CH}}$ for $L/d = 0.8$, at $\Phi \cong 1.0$. Experimental and predicted CH peak locations exhibit reasonable agreement at $\Phi \cong 1.0$, indicating good prediction of strained flame location for a variety of imposed hydrodynamic fields. The variation of flow conditions at constant Φ indicates that the simplified hydrodynamic model can capture the experiment. For the remainder of this study, the scaled separation distance is fixed at $L/d = 0.8$.

To investigate flame-temperature effects, a diluted $\Phi = 0.98$ flame is studied. Excess nitrogen is added to the premixture to reduce the flame temperature. Reasonable agreement was found between measured and predicted velocity and CH profiles, indicating that the simulations can capture variations in flame heat release and attendant temperature-dependent transport effects. The difference between simulated and measured CH peak locations is less than $2\,\delta_{\mathrm{CH}}$.

Flame chemistry effects are probed by varying Φ. Representative results are given in Figs. 7 and 8 that compare experimental and predicted profiles for a lean and rich flame, respectively. For the lean flame ($\Phi = 0.69$), the predicted CH-profile is located upstream of the experimental one, consistent with an overprediction of strained-flame speed. Correspondingly, post-flame velocity is higher than measured.

For the rich flame ($\Phi = 1.31$), good agreement is seen between experiment and simulation. Far from stoichiometry, the results are sensitive to inlet composition. A simulated velocity profile with Φ decreased by 1.4% (the direction required for agreement) is also included in Fig. 7. The 1.4% increment represents the estimated maximum uncertainty in Φ. For lean and rich flames, simulations exhibit high sensitivity to the inlet composition and its measurement uncertainty.

Results for methane-air flames over a range of equivalence ratios are presented in Fig. 9. In an attempt to reduce the number of parameters varied between experiments, strong burning flames ($\Phi \cong 1.1, 1.2$) are diluted with excess nitrogen to maintain an approximately constant flame temperature [22]. This permits a similar strain-field to be established as equivalence ratio is varied, allowing some decoupling of the various effects. We note reasonable agreement for methane-air flames, with a maximum scaled error between measured and predicted CH peak locations of $\approx 2.3\,\delta_{CH}$ for the leanest flame (*cf.* Fig. 9a). Error bars represent the results from simulations with Φ increased and decreased by its maximum estimated uncertainty of 1.4%. For the richest flame ($\Phi = 1.31$), a solution could not be found with Φ increased by 1.4% and the error bar represents a decrease of 1.4% in Φ.

Figure 9b compares experimental and simulated CH profile thicknesses, referenced to the $\Phi = 0.96$ flame. Measured CH-profile thickness is an ensemble average of the FWHM of individual Gaussian fits to single-exposure profiles (60-column average over the flat, central portion of the flame). For the $\Phi = 0.96$, $L/d = 0.8$ flame, the measured CH-profile thickness is approximately twice the simulated value. The Point Spread Function (PSF) of the imaging system and the true CH profile can be approximated by Gaussians. A measured PLIF profile will then also be a Gaussian that is a convolution of the two, with a composite width (squared), δ_{PLIF}^2, that is the sum of the PSF, δ_{PSF}^2, and true CH profile, δ_{CH}^2, widths squared, *i.e.*, $\delta_{PLIF}^2 \cong \delta_{PSF}^2 + \delta_{CH}^2$. PSF width squared is estimated based on the undiluted, $\Phi = 0.96$, $L/d = 0.8$ flame by subtracting the measured and simulated widths squared. This PSF width is systematically applied to study the difference between predicted and measured reference profile thicknesses as a function of equivalence ratio. Figure 9b plots the mean FWHM calculated from multiple shots, $700 < n \leq 1000$, and error bars (one standard deviation). Simulations underpredict variations in δ_{CH} with Φ and dilution. Beam-steering, lensing, or profile-broadening artifacts are estimated not to be significant, or Φ-dependent, and cannot account for this discrepancy.

5. Conclusions

Combined PSV and CH PLIF diagnostics are presented that yield high-accuracy measurements of velocity fields and of the spatial extent of relative CH-concentration profiles. The new PSV implementation requires very low particle loading, resulting in mini-mal flame disturbances and improving statistics in simultaneous PLIF measurements. This implementation and analysis methodology is validated through good agreement with previous laminar flame-speed data and detailed numerical simulations. Numerical simulations overpredict laminar flame speeds for lean flames.

The diagnostic suite facilitates investigation of strained premixed flames, performed here for methane-air mixtures, as a function of the nozzle-plate separation and equivalence ratio. Axial velocity and CH profiles are extracted from PSV and PLIF field data and compared to one-dimensional simulations. Strained flames are simulated using a one-dimensional streamfunction approximation, with detailed chemistry (GRI-Mech 3.0) and multi-component transport. The diagnostics permit a complete boundary-condition specification to the one-dimensional flow-transport-kinetic model, allowing detailed comparisons of measured and predicted velocity and CH profiles in strained stagnation flames.

Near-stoichiometric, strained, methane-air flames are studied, as a function of the nozzle-stagnation plate separation distance, to assess the simplified hydrodynamic model employed. Reasonable agreement is seen for all cases, provided cold-flow (upstream of the flame) boundary conditions are specified from measurements. Flame-temperature effects are probed by nitrogen dilution. Results indicate that the simulations can capture the hydrodynamics, as well as effects caused by variations in flame temperature.

Flames investigated over a range of compositions used both undiluted air-methane mixtures and diluted air-methane mixtures to maintain an approximately constant post-flame temperature rise. Along with the variation in L/d, these preliminary experiments target the convective, transport, and kinetic components of the model. Reasonable agreement is seen for methane-air flames, with the results suggesting that flame strength is slightly overpredicted, especially for lean flames. The results from these preliminary investigations suggest that a complete study would provide further insight.

Acknowledgments

References

[1] P. E. Dimotakis, F. D. Debussy, M. M. Koochesfahani, *Phys. Fluids* 24 (1981) 995–999.

[2] A. A. Adaczyk, L. Rimai, *Exp. Fluids* 6 (1988) 373–380.

[3] C. M. Vagelopoulos, An experimental and numerical study on the stability and propagation of laminar premixed flames, Ph.D. thesis, University of Southern California, 1999.

[4] T. Echekki, M. G. Mungal, *Proc. Combust. Inst.* 23 (1990) 455–461.

[5] G. Sugiyama, *Proc. Combust. Inst.* 25 (1994) 601–608.

[6] D. G. Goodwin, *Proc. of CVD XVI and EuroCVD Fourteen,* Electrochem. Soc., 2003, pp. 155–162.

[7] G. P. Smith, D. M. Golden, M. Frenklach, N. W. Moriarty, B. Eiteneer, M. Goldenberg, C. T. Bowman, R. K. Hanson, S. Song, J. W. C. Gardiner, V. V. Lissianski, Z. Qin, http://www.me.berkeley.edu/gri_mech/.

[8] R. J. Kee, M. E. Coltrin, P. Glarborg, *Chemically reacting flow - theory & practice*. John Wiley & Sons, Inc., New Jersey, 2003.

[9] R. J. Kee, J. A. Miller, G. H. Evans, G. Dixon-Lewis, *Proc. Combust. Inst.* 22 (1988) 1479–1494.

[10] C. K. Law, C. J. Sung, G. Yu, R. L. Axelbaum, *Combust. Flame* 98 (1994) 139–154.

[11] C. J. Sung, C. K. Law, R. L. Axelbaum, *Combust. Sci. Technol.* 99 (1994) 119–132.

[12] C. J. Sung, J. S. Kistler, M. Nishioka, C. K. Law, *Combust. Flame* 105 (1996) 189–201.

[13] C. J. Sung, J. B. Liu, C. K. Law, *Combust. Flame* 106 (1996) 168–183.

[14] J. C. Rolon, D. Veyante, J. P. Martin, F. Durst, *Exp. Fluids* 11 (1991) 313–324.

[15] C. D. Carter, J. M. Donbar, J. F. Driscoll, *Appl. Phys. B* 66 (1998) 129–132.

[16] J. Luque, R. J. H. Klein-Douwel, J. B. Jeffries, D. R. Crosley, *Appl. Phys. B* 71 (2000) 85–94.

[17] J. W. Daily, E. W. Rothe, *Appl. Phys. B* 68 (1999) 131–140.

[18] J. Luque, D. R. Crosley, *LIFBASE: database and spectral simulation program (Version 1.5)*, Report No. MP 99-009, SRI International, 1999.

[19] J. F. Grcar, R. J. Kee, M. D. Smooke, J. A. Miller, *Proc. Combust. Inst.* 21 (1986) 1773–1782.

[20] I. Yamaoka, H. Tsuji, *Proc. Combust. Inst.* 20 (1984) 1883–1892.

[21] C. M. Vagelopoulos, F. N. Egolfopoulos, C. K. Law, *Proc. Combust. Inst.* 25 (1994) 1341–1347.

[22] D. L. Zhu, F. N. Egolfopoulos, C. K. Law, *Proc. Combust. Inst.* 22 (1988) 1537–1545.

Table 1: Experimental conditions

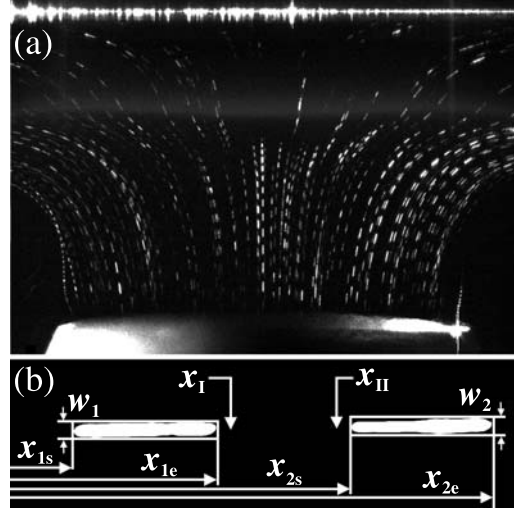|	Φ	L/d	% $O_2 : (O_2 + N_2)$
(a)	0.98	0.6	21.0
	0.96	0.8	21.0
	0.97	1.0	21.0
	0.97	1.2	21.0
(b)	0.98	0.8	18.0
(c)	0.69	0.8	21.0
	0.76	0.8	21.0
	0.87	0.8	21.0
	1.08	0.8	18.0
	1.20	0.8	19.5
	1.31	0.8	21.0

Fig. 1: (a) PSV in a strained premixed methane-air flame (image cropped in the vertical dimension). $\Phi = 0.87$, $L/d = 0.8$. (b) PSV processing implementation.
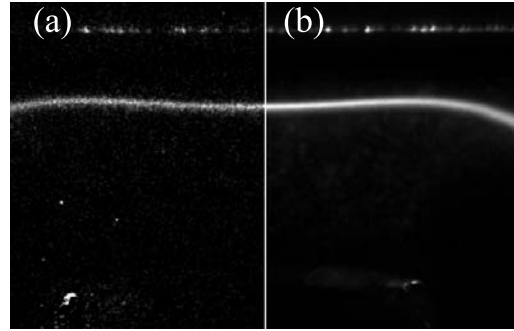

Fig. 2: Example CH PLIF images for a methane-air flame ($344 \times 260\,\mathrm{pix}^2$, $\Phi = 0.96$, $L/d = 0.8$). (a) single exposure. (b) average of 1000 exposures.
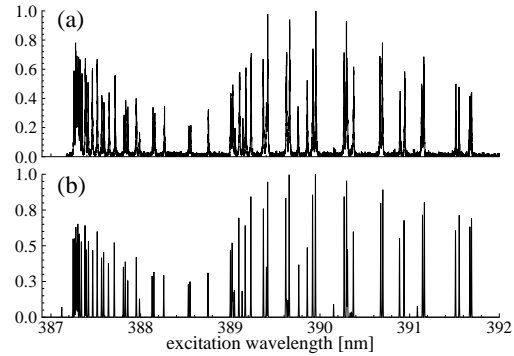

Fig. 3: Normalized experimental and simulated CH fluorescence spectra in a methane-air flame ($\Phi = 0.96$, $L/d = 0.8$). (a) Measured excitation/response scan. (b) Spectrum simulation performed using LIFBASE [18].
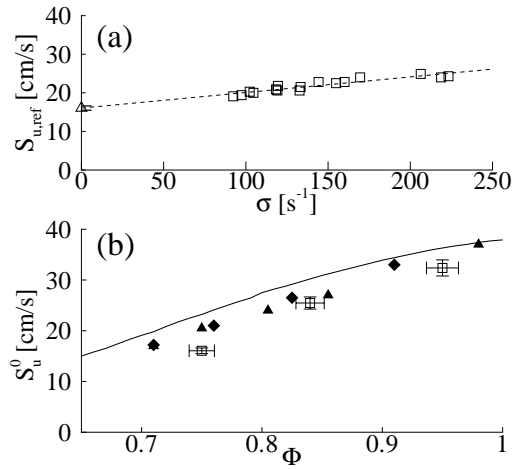
Fig. 4: (a) Flame speeds, $S_{u,ref}$, vs. strain rate, σ, for a $\Phi = 0.75$, methane-air flame. Extrapolation to zero strain rate yields laminar flame speed estimate, S_u^0, and error bar. (b) Estimated laminar flame speeds of methane-air flames (squares). Data by Yamaoka & Tsuji (triangles) [20] and Vagelopoulos *et al.* (diamonds) [21]. Numerical simulations use GRI-Mech 3.0 (line).
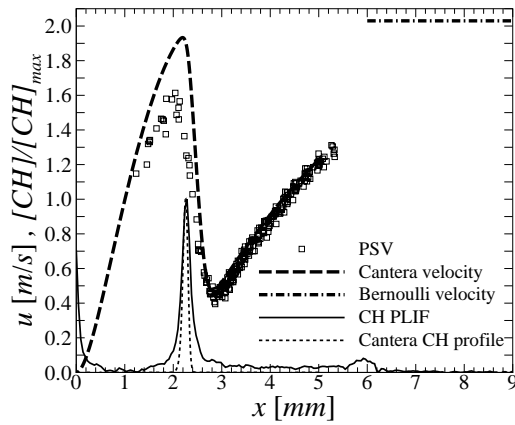

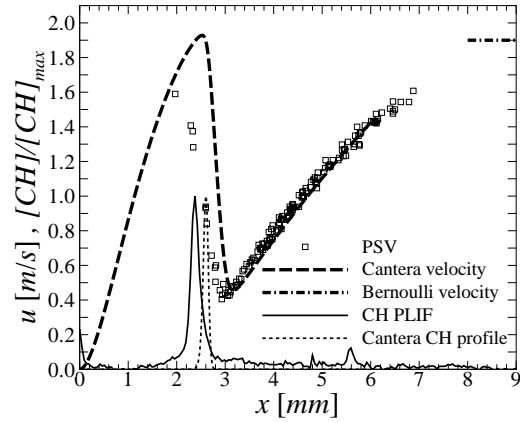Fig. 5: $\Phi = 0.98$, $L/d = 0.6$, methane-air flame profiles. Simulation boundary at $\ell = 5$ mm.

Fig. 6: $\Phi = 0.96$, $L/d = 0.8$, methane-air flame profiles. Simulation boundary at $\ell = 6$ mm.
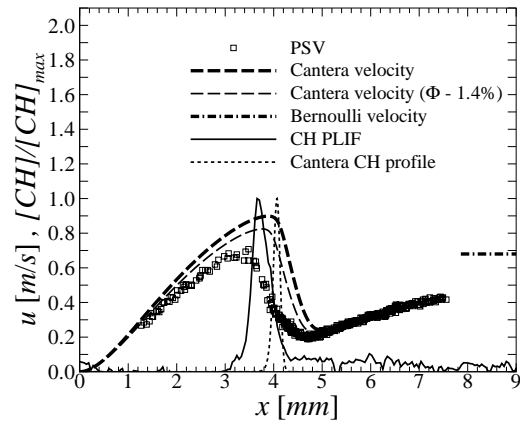

Fig. 7: $\Phi = 0.69$, $L/d = 0.8$, methane-air flame profiles. Simulation boundary at $\ell = 6$ mm.
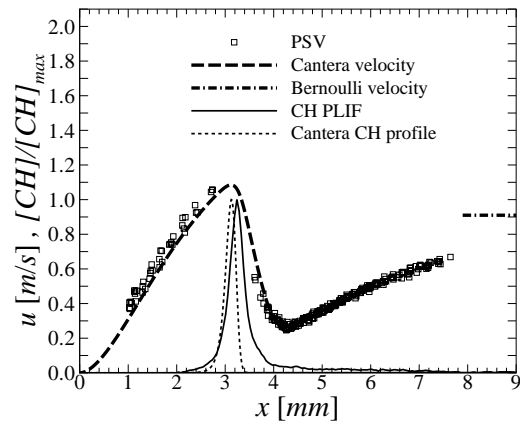

Fig. 8: $\Phi = 1.31$, $L/d = 0.8$, methane-air flame profiles. Simulation boundary at $\ell = 6$ mm.
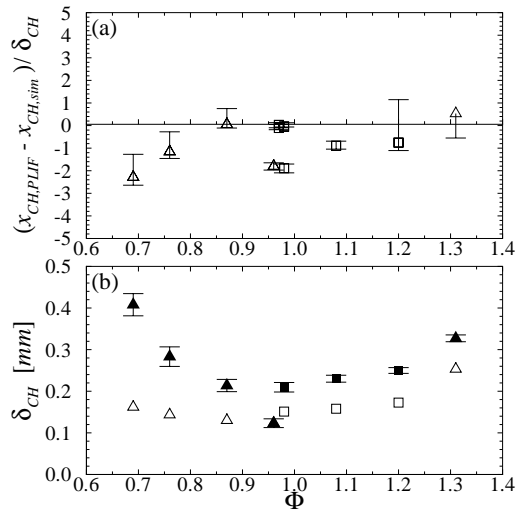
Fig. 9: (a) Difference in measured ($x_{\mathrm{CH,PLIF}}$) and predicted ($x_{\mathrm{CH,sim}}$) peak locations of CH, scaled by the simulated CH profile thickness (δ_{CH}), as a function of equivalence ratio. (b) Experimental (closed) and simulated (open) CH profile thicknesses (FWHM). Experimental data is referenced to the $\Phi = 0.96$ undiluted flame. Undiluted flames marked with triangles; diluted flames with squares.